Magnetic structure and internal field nuclear magnetic resonance of cobalt nanowires

Pascal Scholzen, Guillaume Lang, Andrey S Andreev, Alberto Quintana, James Malloy, Christopher J Jensen, Kai Liu, Jean-Baptiste D'espinose de Lacaillerie

Magnetic structure and internal field nuclear magnetic resonance of cobalt nanowires

*Pascal Scholzen,[1] Guillaume Lang,[2] Andrey S. Andreev,[3] Alberto Quintana,[4†] James Malloy,[4] Christopher J. Jensen,[4] Kai Liu,[4] and Jean-Baptiste d'Espinose de Lacaillerie[1]**

(1) Soft Matter Science and Engineering, ESPCI Paris, Université PSL, UMR CNRS 7615, Sorbonne Université, 75005 Paris, France.

(2) Laboratoire de Physique et d'Étude des Matériaux, UMR CNRS 8213, ESPCI Paris, Université PSL, Sorbonne Université, 75005 Paris, France.

(3) TotalEnergies One Tech Belgium (TEOTB), Zone Industrielle C, 7181 Feluy, Belgium

(4) Physics Department, Georgetown University, Washington, DC 20057, USA

KEYWORDS. ^{59}Co NMR, internal field NMR, ferromagnetism, metallic nanostructures, nanomagnetism, FNR.

ABSTRACT:

The magnetic properties of cobalt metal nanowires grown by electrodeposition in porous membranes depend largely on the synthesis conditions. Here, we focus on the role of electrolyte additives on the magnetic anisotropy of the electrodeposited nanowires. Through magnetometry and internal field nuclear magnetic resonance (IF NMR) studies, we compared both the magnetic and crystalline structures of 50 and 200 nm diameter Co nanowires synthesized in presence or absence of organic additives. The spectral characteristics of IF NMR were compared structurally to x-ray diffraction patterns, and the anisotropy of the NMR enhancement factor in ferromagnetic multidomain structures to magnetometry results. While the magnetic behavior of the 50 nm nanowires was dominated, as expected, by shape anisotropy with magnetic domains oriented on axis, the analysis of the 200 nm proved to be more complex. ^{59}Co IF NMR revealed that the determining difference between the samples electrodeposited in presence or in absence of organic additives was not the dominant crystalline system (*fcc* or *hcp*) but the coherent domain sizes and boundaries. In the presence of organic additives, the cobalt crystal domains are smaller and with defective grain boundaries, as revealed by resonances below 210 MHz. This prevented the development in the Co *hcp* part of the sample of the strong magnetocrystalline anisotropy that was observed in the absence of organic additives. In the presence of organic additives, even in nanowires as wide as 200 nm, the magnetic behavior remained determined by the shape anisotropy with a positive effective magnetic anisotropy and strong anisotropy of the NMR enhancement factor.

1. INTRODUCTION

Ferromagnetic nanowires with tunable magnetic properties have been the focus of intense research efforts, not only because they raise interesting fundamental physics questions but also because of their technological relevance.[1,2] For example, they can be used for ultra-high density magnetic recording,[3] in magnetic field sensors or random-access memories exploiting the giant magnetoresistance observed in the case of multilayered nanowires.[4–7] Recently, ferromagnetic nanowires have attracted interest in curvature-induced topologically protected magnetization textures,[8,9] as well as prototype structures for 3D information storage.[10] Electrodeposition is a cost-effective and versatile technique that allows for easy and broad tuning of microstructures by simply adjusting growth parameters or electrolyte recipes.[11,12] Progress in producing arrays of ferromagnetic materials by electrodeposition into porous membranes made of polycarbonate (PC) or anodized aluminum oxide (AAO) has stimulated research by providing model systems to study the structural and electromagnetic properties of metallic nanowire assemblies.[10,13–16]

Of particular interest is the issue of domain wall structure and dynamics. In soft magnetic nanowires, magnetic domain walls form perpendicularly to the wire axis and can propagate collectively along the wire under the drive of magnetic fields,[17] spin-polarized currents[18] or electric fields.[19] This property lies at the basis of racetrack memory devices.[20] Most studies so far have explored the dynamic and static structures of domains and domain walls by magnetometry,[10,21,22] pulsed resistometry[23–25] and magnetic imaging.[18,26–29] In this work however, we probed the magnetic structure of arrays of parallel cobalt nanowires by ^{59}Co internal field nuclear magnetic resonance (IF NMR), with a particular focus on the domain wall response to radiofrequency (*rf)* fields. This particular form of solid-state NMR is as old as NMR itself[30] but

has raised a renewed interest because to its ability to probe cobalt nanoparticles in catalysts or battery materials.[31–33]

In contrast to diamagnetic/paramagnetic materials, conventional (Zeeman) solid-state NMR is not suited to studying ferromagnetic materials and instead, it is the internal hyperfine field inside these structures that is responsible for lifting the degeneracy of the nuclear spin levels. For the study of (ferromagnetic) cobalt nanowires, internal field (IF) NMR thus represents a well-adapted technique due to the possibility to simultaneously analyze the crystalline and magnetic properties of the samples.

Strijkers et al.[34] successfully adopted this approach to determine the crystalline structure and crystal orientation inside cobalt wire samples, as well as the influence of the dipole-dipole interactions on the magnetic structure. For this, they used a combination of experiments at zero field and in the presence of an external field oriented parallel or perpendicular to the wire axis. Others have addressed nanowires made of pure cobalt as well as Co-Cu alloys and multilayers.[35–38] In combination with x-ray diffraction (XRD) measurements, they studied the crystalline structure of those three kinds of samples for different synthesis parameters. They found that a fast deposition rate favors the appearance of a *fcc* crystalline structure, while a pure *hcp* phase is formed using slow deposition rates.

Nevertheless, in cobalt nanowires, how synthesis conditions determine precisely the magnetic domain structure inside the wires remains an open question. In this paper, we study the magnetic and crystalline structures of cobalt nanowires electrodeposited inside the 50 nm and 200 nm cylindrical pores of PC and AAO membranes, respectively. The samples were studied by IF NMR experiments (without an applied field), supported by XRD, scanning electron microscopy

(SEM) and magnetometry as complementary experiments. The first goal was to obtain new information on the crystalline and magnetic structure for nanowires obtained with different electrodeposition conditions, focusing on the influence of additives. Secondly, we wished to exemplify the methodological potential of simple IF NMR experiments in strongly anisotropic ferromagnetic structures, such as nanowires. The NMR spectral features complemented XRD for crystalline phase determination, while the analysis of the anisotropy of the enhancement of the *rf* field revealed the orientation of the magnetic domains inside the nanowires.

2. MATERIALS AND METHODS

Sample Synthesis. All reagents have been used without any further purification: Cobalt sulfate heptahydrate ($CoSO_4 \cdot 7H_2O$ ReagentPlus ≥99%), Cobalt chloride hexahydrate ($CoCl_2 \cdot 6H_2O$ ACS reagent, 98%), Boric Acid (H_3BO_3 ACS reagent, ≥99.5%), Polyethylene Glycol (PEG – Mn 20000), 1-(2-Hydroxyethyl)-2-Imidazolidinethione ($C_5H_{10}N_2OS$), Thioglycolic Acid ($C_2H_4O_2S$ ≥98%), Janus Green B (3-Diethylamino-7-(4-dimethylaminophenylazo)-5-phenylphenazinium chloride.

Cobalt nanowires of 50 nm and 200 nm diameter were synthesized by template-assisted electrodeposition using a Princeton Applied Research Potentiostat 263A. For the 50 nm diameter nanowires, 6μm thick track-etched polycarbonate membranes (PC) with a pore density of 6×10^8 cm^{-2} were used,[39] after coating with Au back electrodes. For the 200 nm diameter nanowires, 60 μm thick anodized aluminum oxide (AAO) membranes with a pore density of 10^9 cm^{-2} were used,[40] after coating with Cu back electrodes.

Electrolytes formulation used in this project were adapted from prior studies.[5,40,41] For the additive-free electrolyte, a Watts-like[42] electrolyte with Ni replaced by Co precursors was employed. Specifically, the electrolyte was composed of 240 g/L $CoSO_4 \cdot 7H_2O$ + 50 g/L $CoCl_2 \cdot 6H_2O$ + 40 g/L H_3BO_3. For the additive-containing electrolyte, the same recipe as the additive-free solution was used, with the addition of a mixture of 60 mg/L PEG + 34 μg/L Janus Green B + 34 μg/L 1-(2-Hydroxyethyl)-2-Imidazolidinethione + 12 μg/L Thioglycolic Acid. In both solutions, pH was left unaltered and neither of the solutions were deaerated nor stirred prior to or during the growth. All samples were grown potentiostatically at -1.1V relative to an Ag^+/AgCl reference electrode. Deposition time was controlled to avoid overplating. After the synthesis, the Cu back electrodes on the AAO membranes were etched away using 2M $FeCl_3$, while the Au electrodes on PC membranes were not removed.

In summary, using the same electrodeposition method for each of the two diameters under consideration, Co nanowires were grown with and without additives resulting in a total of four samples.

SEM. Scanning Electron Microscopy images were obtained on two different microscopes. The two 200 nm AAO samples were imaged on a Magellan 400 (ThermoFisher Scientific, USA) in a high vacuum. The 50 nm PC sample was analyzed on a Quattro ThermoFisher under a 100 Pa water vapor atmosphere, in order to avoid charge accumulation at the sample surface due to the lower cobalt content of the sample. Both instruments were used in secondary electron mode with a Field Emission Gun at a voltage of 5 kV.

XRD. X-ray diffraction was performed using a X'Pert (Philips) diffractometer with a PW3050 (θ/2θ) goniometer between 35° and 100° and with Cu as the anode material operated at 40 mA,

40 kV. The samples were positioned with the plane of the membrane in the reflection plane of the XRD experiment. As a result, it is mainly the crystallographic planes perpendicular to the wire axis that diffracted, as shown in **Figure 1**, with small deviations expected due to imperfect alignment of the pores in the membranes. The ICDD reference files for spectra corresponding to *fcc* and *hcp* Co are PDF cards No. 00-015-0806 and 00-005-0727, respectively. Note that the gold electrode remaining on the 50 nm PC sample saturated the signal, masking the cobalt nanowire signal. As a result, no structural analysis of the cobalt by XRD could be performed on this sample.

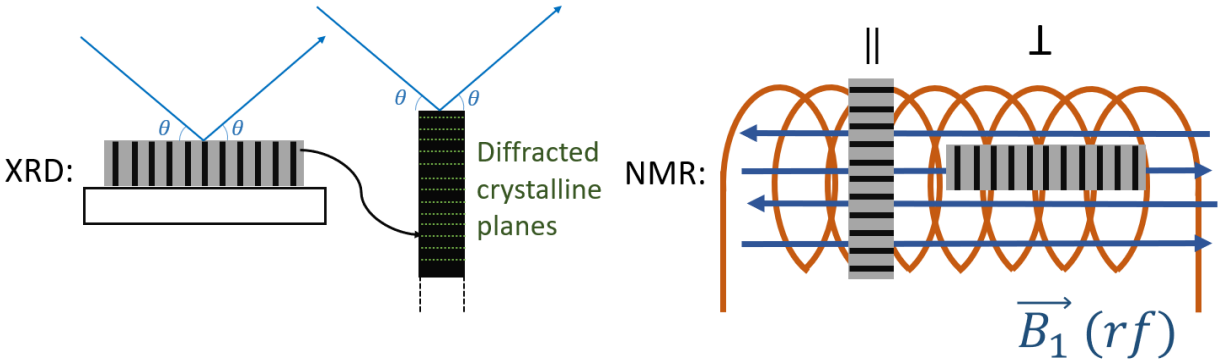

Figure 1. Schematic representation of the XRD and IF NMR experimental geometries. The membrane templates are shown in grey and the cobalt nanowires in black. XRD: The membrane sample was situated in the diffraction plane, i.e., diffraction came mainly from the crystallographic planes parallel to the membrane, or perpendicular to the wire axis. NMR: The samples were tested with two different orientations between the wire axis and the axis of the excitation and pick-up coil: Parallel (||) and Perpendicular (⊥) to the excitation magnetic field B_1 inside the coil.

^{59}Co IF NMR. All NMR experiments were carried out at zero external field, using a SCOUT spectrometer (TECMAG, USA) and a commercial static broadband probe with a 5 mm solenoid excitation/pick-up coil (NMR-Service, Germany). Although the experiments were performed at ambient temperature, the probe was inserted inside a cryostat (Oxford Instruments, UK) for *rf* shielding purposes. The spectra were acquired point-by-point using spin-echo with frequency steps of 0.5 MHz. The spin-echo sequence was composed of two equal *rf* pulses of 1 μs with an interpulse delay of 8 μs. The repetition rate of the sequence was 67 Hz, thanks to the very short relaxation time of ferromagnetic cobalt, and the number of transients per point was equal to 4 k. In order to obtain quantitative spectra, the pulse power was varied over 20 dB (i.e., over two orders of magnitude for the *rf* power or one order of magnitude for the *rf* field B_1 amplitude) at each frequency point. The signal from the pulse power giving the maximum signal intensity at each frequency was chosen and used for the spectrum. The lower this power for a certain frequency, the higher the so-called enhancement factor and *vice-versa*. The enhancement factor is defined by the ratio of the excitation field seen by the nuclear spins during an impulsion and the magnitude of the *rf* field itself and allows to obtain additional information about the cobalt magnetic structure.[43,44] In order to quantify the pulse power, the peak voltage was measured using an oscilloscope, which allowed to calculate the effective pulse power. The T_2 relaxation time at the main peaks was estimated by varying the interpulse delay and the spectral intensities over the whole spectrum were corrected accordingly as well as for the frequency (ω^2) dependence of the signal intensity. An overview of the measured relaxation times is given in the Supplementary information (Table S3). The corrected spectra were fitted using the DMFIT program.[45] The peak attribution is described in the upcoming section of this work and more details about the fitting procedure can be found in the Supplementary information (Table S4).

To facilitate their insertion in a glass NMR tube fitting the 5 mm coil, the membranes containing the nanowires were cut into strips. In the case of the 200 nm AAO samples, the quantity of Co inside a single strip was already sufficiently high to obtain a good NMR signal. This was not the case for the 50 nm nanowire samples which have smaller nanowires with a lower density, and for which six of the membrane strips were stacked inside the NMR tube. As the orientation of the excitation field with respect to the wire main axis is crucial, each sample was tested at two different orientations, as shown in Figure 1. Since the nanowires are oriented normal to the membrane, for the first orientation, called *parallel*, the membranes were put perpendicular to the coil axis. This corresponded to a parallel orientation of the nanowire axis with respect to the excitation field. Similarly, for the *perpendicular* orientation, the membranes were placed parallel to the coil axis.

Magnetic characterization. Magnetic properties of the synthesized samples were studied by vibrating sample magnetometry (VSM) using a Princeton Measurement Corporation MicroMag 3900, as well as a Quantum Design Materials Property Measurement System (MPMS3). Hysteresis loops were measured at room temperature with an external field, up to 1.8 T, applied either parallel or perpendicular to the wire axis.

3. RESULTS

SEM. In order to verify the pore diameter, spacing and regularity, SEM analysis was performed on the samples. As shown in the tilted view of Figure 2a, the 200 nm pores inside the AAO samples were not completely filled with cobalt, in order to avoid overplating. In addition, the upper end of the pores, close to membrane surface, seemed to be quite defaulted due to a

damaged surface, which was without consequence because of their incomplete filling. The AAO membranes, produced by anodic oxidation of aluminum in acidic solution, had interpore separations smaller than the pore diameter. On the other hand, as shown in Figure 2b, the 50 nm pores inside the PC membranes, being produced by track etching, had interpore spacings that were on average much larger than the pore diameter.

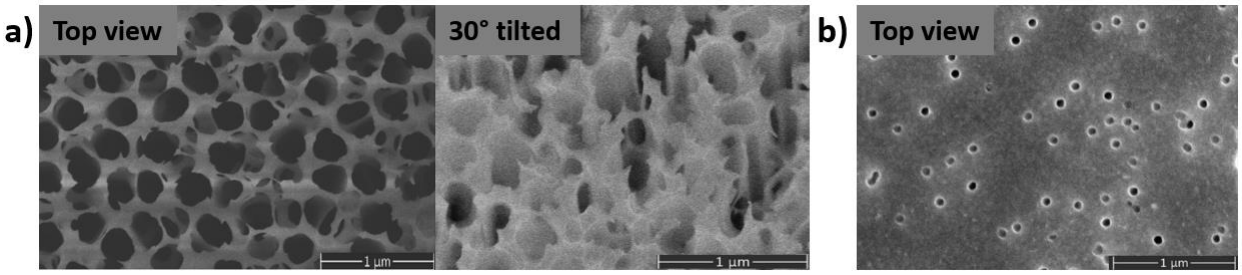

Figure 2. SEM images for two different membrane samples filled with cobalt nanowires. a) 200 nm AAO membrane sample under high vacuum (top view and 30° tilted with respect to the top view). b) 50 nm PC membrane sample under a 100 Pa vapor pressure atmosphere.

XRD. The XRD patterns of the two 200 nm samples grown in AAO membranes (with and without additives) are represented in Figure 3.

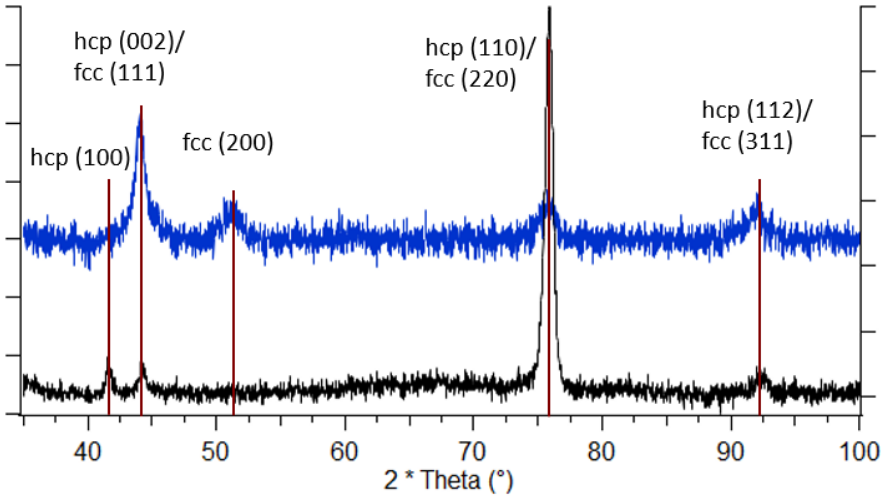

Figure 3. XRD patterns collected on 200 nm Co nanowires grown in AAO membranes (top/blue: with; bottom/black: without organic additives). The samples are analyzed with the membrane plane being in the XRD diffraction plane.

There have been numerous studies in the literature discussing the correlation between additive use and sample microstructure.[46–48] Here, all the observed peaks in the diffraction pattern are from cobalt, either in the *fcc* or *hcp* phase. Three peaks are observed around 44.3°, 75.9° and 92.4°, which can be assigned to either *fcc* or *hcp*, irrespective of the presence of organic additives in the electrolyte during electrodeposition or not. In the reference files, the theoretical positions of the cobalt *fcc* (111) and *hcp* (002) reflections are 44.2° and 44.8°, respectively, suggesting that the 44.3° peak mainly came from *fcc* Co. Nevertheless, even a significant contribution to this peak from *hcp* Co cannot be excluded. Besides these three peaks, a fourth peak around 51.5° is observed in the diffraction pattern of the sample synthesized with additives and can unambiguously be assigned to *fcc* Co (200). While this peak is not present for the sample without additives, another peak at 41.6° is observed that corresponded this time unambiguously to *hcp* Co (100). These observations suggest that the additives changed the main crystalline form

of the wire from *hcp* to *fcc*-rich. Further useful information could also be drawn about the crystal orientation with respect to the wire axis, as exposed earlier when describing the XRD setup (Figure 1). This is particularly interesting in the case of *hcp* cobalt in order to determine the relative orientation of the *c*-axis with respect to the wire axis because the *c*-axis is the magnetic easy-axis of *hcp* Co. The *hcp* Co parts of the samples without organic additives were oriented with the *c*-axis mainly perpendicular to the wire axis since the relative intensity of the peaks corresponding to *hcp* Co (110) vs. *hcp* Co (002) is significantly higher than in polycrystalline samples.

When comparing the FWHM of the reflections of the 200 nm samples electrodeposited with and without additives, it can be seen that the reflections obtained from the former were broader than the ones obtained from the latter, indicating a smaller crystallite size due to the presence of the additives during electrodeposition. The crystallite size in both samples was estimated using Scherrer's formula based on the FWHM of the peaks in the corresponding diffractograms in Figure 3 (more details about Scherrer's formula can be found in the Supporting Information). As most of the peaks are potentially composed of two overlapping peaks corresponding to *hcp* and *fcc* Co, only the peaks around 51.5° (*fcc* Co (200)) and 41.6° (*hcp* Co (100)) can be considered when estimating the crystallite size inside the sample synthesized without and with additives, respectively. The FWHM of the peak observed at 51.5° is around 1.9°, indicating a crystallite size of around 5 nm for the sample synthesized with additives. It is noteworthy that the other peaks in the corresponding diffractogram are all thinner than this peak, therefore the average crystallite size of 5 nm was a lower limit. When analyzing the diffractogram of the sample synthesized without additives, it can be seen that the FWHM of the peak observed at 41.6° is around 0.42°, indicating a crystallite size of around 24 nm in this sample. In this case, all the

other peaks in the corresponding diffractogram are broader than this peak, meaning that the average crystallite size of the sample might be smaller than 24 nm, but the potential overlap of different peaks does not allow a precise crystallite size determination.

The XRD spectrum of the 50 nm PC membrane sample can be found in the Supporting Information (Figure S1). Unfortunately, the reflections from the gold electrode still attached to the membrane masked those from cobalt and consequently, no conclusions could be drawn regarding the crystalline structure and the average crystallite size of this sample.

Magnetic hysteresis measurement. The magnetic properties of the wires were studied at room temperature with a magnetic field applied perpendicularly (⊥) or parallel (||) to the wire axis, as shown in Figure 4 and S3.

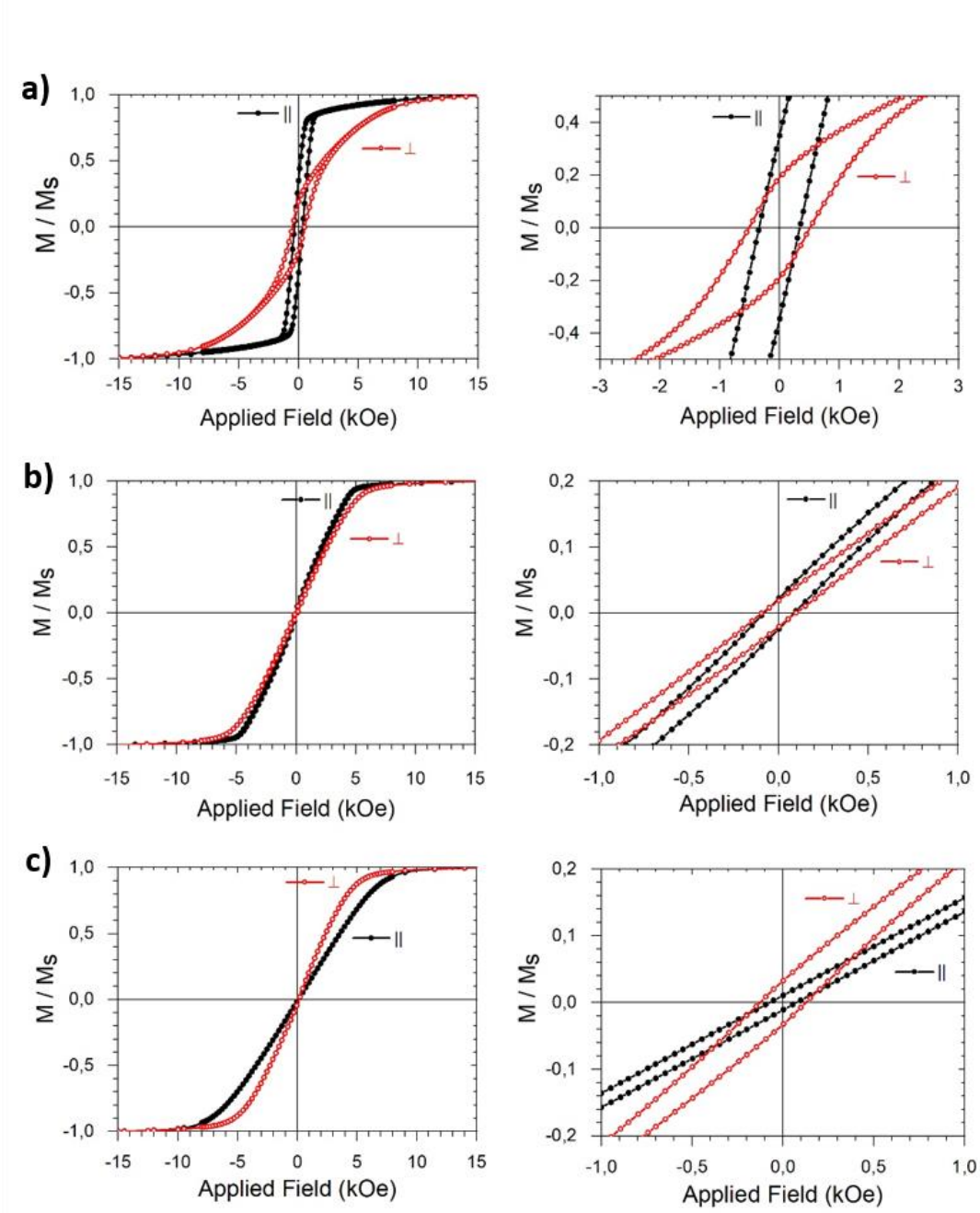

Figure 4. Magnetic hysteresis loops recorded at ambient temperature with the field applied perpendicular (⊥, red hollow symbols) or parallel (||, black full symbols) to the cobalt wires. a) 50 nm Co nanowires grown in a PC membrane with additives, b) 200 nm Co nanowires grown in AAO membranes with additives, and c) 200 nm Co nanowires grown in AAO membranes without additives in electrolyte. The magnetic loop of the 50 nm sample grown without additives

was very similar to the one with additives. For clarity, it is shown in Supporting information Figure S3. Left: full loops. Right: Zoom-in views of the full loops.

The 50 nm Co nanowires grown in a PC membrane exhibited very similar squared hysteresis loops regardless of the presence of organic additives. The coercivity of about 500 Oe when measured on-axis (i.e. parallel), was about an order of magnitude larger than that in typical Co films. This coercivity enhancement is due to the small nanowire diameter, which impedes the domain wall propagation mechanism during magnetization reversal.[49–51] The magnetic easy axis of the wires can be determined by comparing the applied magnetic fields needed for saturation for the different directions of the applied field.

A clear magnetic easy axis parallel (positive magnetic anisotropy) to the nanowires is observed for the 50 nm sample, due to the shape anisotropy resulting from the strong saturation field ($2\pi M_S$) of 8.8 kOe required to orient the magnetization away from the wire axis (Figure 4a).[27] In the 200 nm Co nanowire samples grown in AAO membranes, the magnetic properties exhibited significant differences. The coercivity enhancement was reduced to values below 120 Oe, due to the larger nanowire diameters. It is well known that a large diameter favors the formation of domain walls along the wire axis thus degrading coercivity.[52] Wall motion occurring during magnetization reversal can be affected by several parameters such as pinning or metal-insulator stress interfaces,[50] but everything else equal, coercivity is expected, as observed here, to vary linearly with the ration of magnetic anisotropy to magnetization.[53] Furthermore, when cobalt was electrodeposited in the presence of additives, i.e. *fcc*-rich according to XRD, the nanowire axis (parallel geometry) was still the magnetic easy axis. However, its difference with the perpendicular geometry was much smaller (Figure 4b), as the much closer spacing between nanowires leads to strong dipolar interaction that prefers antiferromagnetic alignment.[10,54,55] In

contrast, the *hcp*-rich 200 nm sample, synthesized without additives, exhibited a magnetic easy axis perpendicular to the wire axis (negative magnetic anisotropy) (Figure 4c). This is a manifestation of the *hcp* c-axis being perpendicular to the nanowires[56,57], as suggested by the XRD diffraction patterns of Figure 3.

Internal field NMR. In metallic cobalt structures, valuable information may be obtained from the IF NMR spectrum, such as the crystalline and magnetic structure. Although not as commonly used as XRD or magnetometry, it nicely complements these methods due to its very local (nanoscale) character. The general spectral features of IF NMR in *fcc* or *hcp* cobalt nanostructures are as follows. At room temperature, the peak around 213 MHz can be assigned to signal coming from ^{59}Co nuclei in *fcc* multidomain structures.[30,32] By symmetry of the *fcc* structure, this peak is generally narrow and well defined. A small peak around 216 MHz can be distinguished, which is in the literature sometimes assigned to Co in a single-domain magnetic structures, with the difference compared to the multidomain *fcc* being due to the demagnetizing field effect.[32,58] However, this peak assignment is generally done when analyzing Co nanoparticles and not for oriented systems like nanowires. In nanowires the form factor is not the same one as in spheres[59] and consequently the demagnetizing field would lead to a different frequency shift in single-domain *fcc*. Possible origins of this peak could therefore be *fcc* stacking faults with a higher internal field compared to pure *fcc*[60,61] or *fcc* structures with a residual demagnetizing field. The signal coming from anisotropic *hcp* structures is generally much broader than the one corresponding to *fcc*. A broad peak between 217 MHz and 222 MHz is often assigned to *hcp* cobalt without distinction between signal arising from mono- and multidomain structures.[32,62,63] Additional information about the magnetic structure can be obtained from the variation of the optimal power with frequency, which is inversely proportional

to the enhancement factor. As the enhancement is much stronger for nuclei situated inside a domain-wall structure than for those inside the domain itself, less power is needed for the optimal excitation of the former.[43,44,62] In a similar fashion, the signal arising from ^{59}Co nuclei inside domain walls will also be enhanced much more than from the ones inside the domains, which means that the main signal observed when analyzing multidomain structures will be from the excitation of the domain walls and not from the domains.[43,64]

Figure 5 displays the IF NMR spectra in the frequency range associated with ^{59}Co resonances. For all samples, the spectral features were similar and supported the conclusion that both *hcp* and *fcc* structures coexisted (Figure 5a-c). While the XRD analysis suggests the presence of *fcc* or *hcp*-rich structures in the 200 nm samples, depending on the presence of additives in the electrolyte during the wire deposition or not, this difference was not apparent by NMR.

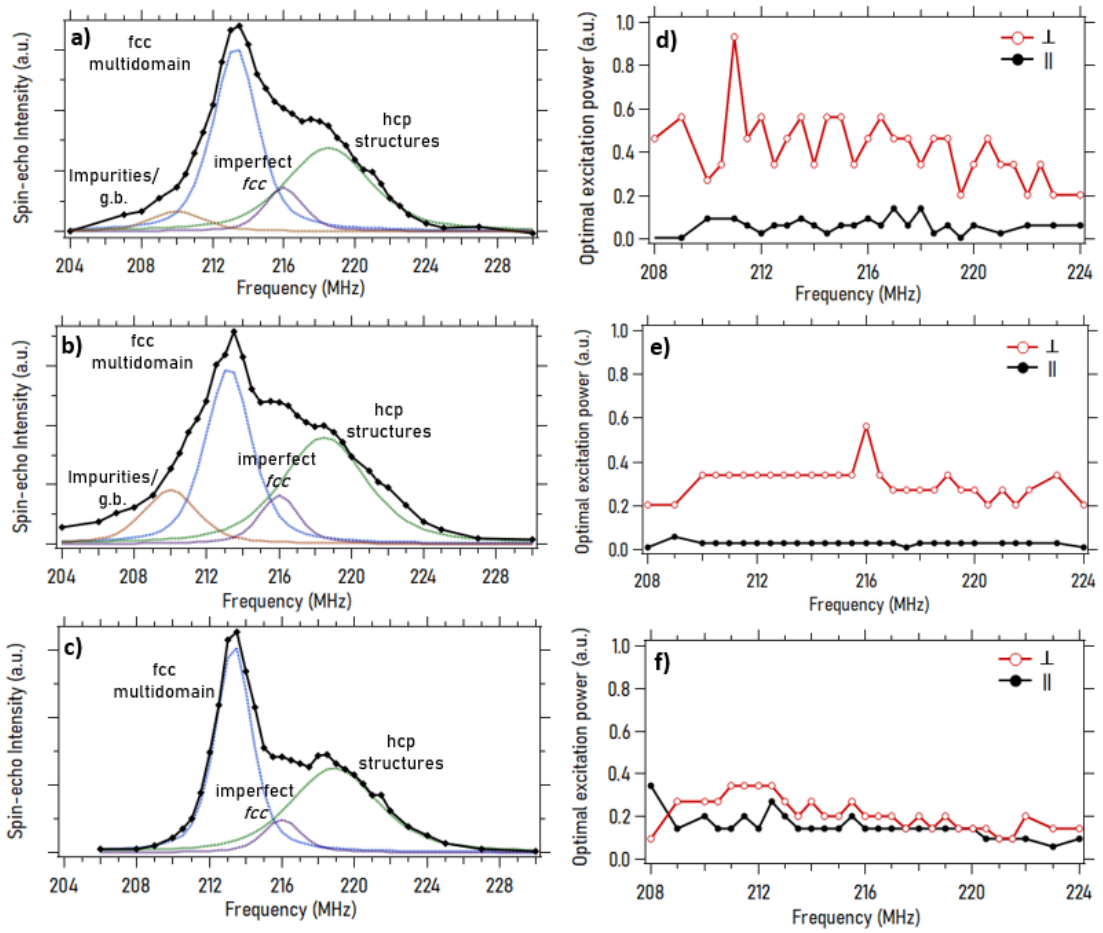

Figure 5. ^{59}Co IF NMR room temperature spectra: a) 50 nm Co nanowires grown in PC membrane, b) 200 nm Co nanowires grown in AAO membranes with organic additives (XRD *fcc*-rich), and c) 200 nm Co nanowires grown in AAO membranes without organic additives (XRD *hcp*-rich). A tentative decomposition into peaks corresponding to different crystalline and magnetic structures is also presented (g.b. = grain boundaries). The spectral shape is identical regardless of the orientation between the *rf* pulse and the wire axis, so only one orientation is represented here. The numerical comparison of the decomposition and the corresponding fitting parameters can be found in the Supporting Information (Figure S5, Table S4). The graphs d), e) and f) correspond to the optimal excitation power for each of the left-side graphs for different orientations: The red line (hollow spheres) corresponds to a perpendicular (⊥) orientation

between the direction of the *rf* pulse and the wire axis, the black line (full spheres) to a parallel (||) one.

Indeed, in all cases, a significant resonance in the 217-222 MHz range together with a peak around 213 MHz revealed the presence of both *hcp* and *fcc* components, with similar weights for both samples (The comparison of the weights in the decomposition can be found in the Supporting Information (Figure S5). The distribution of the optimal power, and hence of the enhancement factor, was constant over the whole spectrum range for all studied samples (Figure 5d-f). No distinction in that respect could be made between the 213 MHz resonance of the *fcc* multidomain structures and the rest of the spectra. One could thus conclude that most of the signal in the spectrum, also in the *hcp* Co part, arose from the excitation of the walls in multidomain structures, establishing that the magnetic structure of the nanowires was broken up into magnetic domains. The signal was dominated by the excitation of the domain walls.[43,64] A significant difference between the spectra obtained from samples synthesized in presence (Figure 5a-b) and in absence (Figure 5c) of organic additives is the occurrence of a signal at frequencies below the main peak for the samples synthesized with additives. Such a signal in usually attributed to arise from grain boundaries, impurities or interfaces [61,65] and can be fitted quite well with one peak around 210 MHz in the present spectra.

Experiments with different radio frequency (*rf*) field orientations relative to the wire axis have been performed, but the shape of the resulting spectra was identical for both orientations for all analyzed samples. However, a change in the power needed for an optimal excitation could be observed for some samples. For the samples for which the VSM measurements revealed a magnetic easy axis parallel to the wire axis (50 nm Co wires & 200 nm wires grown with additive), the enhancement factor (inversely related to the optimal power) was stronger for the *rf*

field *parallel* to the wire axis than for the *perpendicular* orientation (Figure 5d-e). In contrast, the 200 nm Co wires grown without additives, for which VSM revealed an easy axis perpendicular to the wire axis, had a similar enhancement factor for both orientations (Figure 5f). These results provided more information on the magnetic domain structure, as will be discussed in the following section.

4. DISCUSSIONS

From XRD and magnetometry measurements, it was apparent that the samples had different crystalline and therefore magnetic structures. Concerning the crystalline structure, XRD suggested that the 200 nm nanowires produced with organic additives had an enriched *fcc* structure, while the 200 nm nanowires produced without organic additives had a *hcp*-rich structure with a *c*-axis perpendicular to the wire axis. However, due to the oriented character of the sample during the XRD experiments and the overlapping of the main *fcc* and *hcp* Co peaks, a quantitative phase determination was not unambiguously possible. In addition, XRD experiments only detect signal coming from relatively large cobalt coherent domains, while NMR is sensible to the whole sample. Indeed, the IF NMR spectra revealed that, at the nanoscale, both crystalline structures were present in more or less the same relative amount.

Concerning the magnetic structures, magnetometry and IF NMR results supported each other. The M(H) hysteretic behavior has already been observed in previous articles analyzing cobalt wires of different diameters inside track-etched polymer membranes.[10,27,34] The physical basis for the observed magnetic anisotropy of soft ferromagnetic materials is well known.[66] It results from the superposition of shape anisotropy, magnetocrystalline anisotropy and wire-wire interactions (see for example the discussions of magnetic anisotropy in Co nanowires in references [27,34]).

Since the nanowire shape anisotropy favors a magnetization alongside the wire axis, this is the preferred configuration for wires with a weakly anisotropic crystalline structure, like *fcc* cobalt. On the other hand, a strong crystalline anisotropy (like *hcp* Co) perpendicular to the wire axis will be in competition with the shape anisotropy, possibly leading to a magnetic easy axis perpendicular to the wires.[56,57,67,68]

The case of the Co nanowires with a relatively narrow diameter of 50 nm grown in a PC membrane was the most straightforward as it was dominated by shape anisotropy. In this instance, the dipolar field acting on a wire due to its neighbors can safely be neglected because of the large interwire distances. Furthermore, the small 50 nm diameter, combined with the µm-scale wire length, resulted in a strong shape anisotropy[27,34], as reflected in the saturation field difference of the sample (Figure 4a). It could be inferred that at zero field, the magnetic structure, confined by the wire diameter, was broken up into magnetic domains with on-axis remanent magnetic moments. This conclusion was strongly supported by the anisotropy of the IF NMR enhancement factor as function of the orientation of the wire axis to the excitation field (Figure 5d). It must be recalled that the flat frequency dispersion of the enhancement factor established that the IF NMR signal of our samples arose predominantly from the excitation of domain walls. In this case, the enhancement factor finds its origin in the periodic displacement of the domain walls under the effect of the *rf* field**,** a displacement which is favored when the field is oriented along the domain magnetization[43], as represented schematically in Figure 6a. *Rf* fields with a different orientation compared to the domain axes will displace the walls less efficiently.[69] Consequently, the higher enhancement recorded when the *rf* field was applied on axis with the nanowires supported the conclusions that the magnetic domains were magnetized along the wires. Note that the same experiments have been performed on 50 nm wires deposited without

the presence of organic additives in the electrolyte, leading to the same results regarding the magnetic anisotropy (Supporting Information Figure S3 & S4). In contrast, the magnetic properties of the 200 nm samples strongly depended on the synthesis conditions, indicating that the magnetic behavior of the 50 nm wires is controlled indeed by the shape anisotropy.

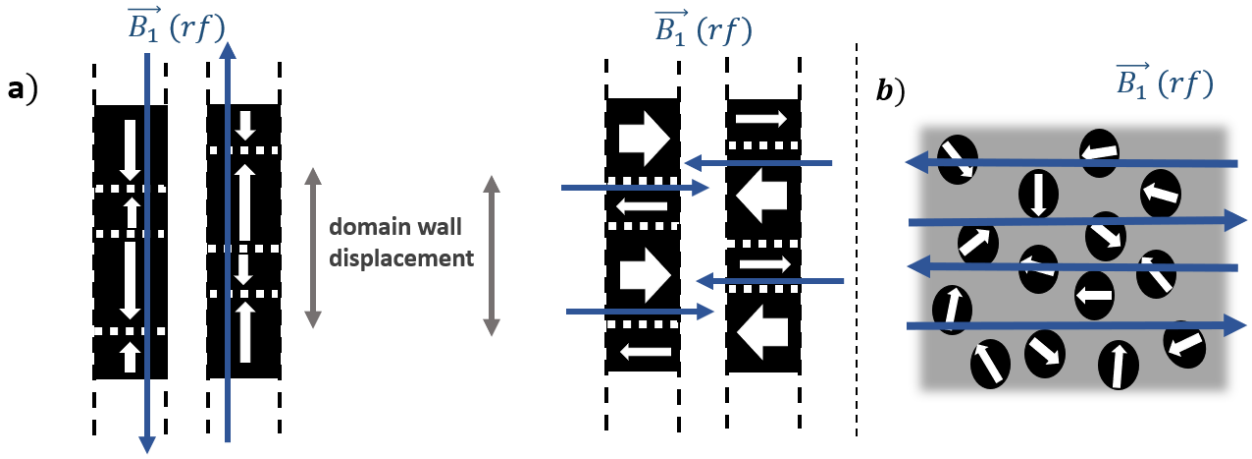

Figure 6. a) Orientation of the optimal excitation field as function of the domain wall structure. A *rf* field (B_1) with this orientation will efficiently displace the domain walls back and forth by favoring the growth of domains, as shown schematically. Left: domains alongside the wire axis: 50 nm & 200 nm nanowires with additives. Right: domains perpendicular to the wire axis: 200 nm without additives. b) Random orientations of the in-plane magnetic domains for the sample without additives, which are therefore more or less aligned with the orientation of the *rf* field perpendicular to the wire axis.

For the two samples of 200 nm Co nanowires grown in AAO membranes, the same analysis could be performed. For the sample electrodeposited in presence of additives in the electrolyte,

the enhancement factor was higher for a *rf* field orientation along the wire axis **(**Figure 5e), consistent with the magnetic easy axis along the nanowires detected by VSM (Figure 4b). In contrast, for the 200 nm sample electrodeposited without additives, VSM revealed a magnetic easy axis perpendicular to the nanowires (Figure 4c), while the enhancement factor did not reveal any strong anisotropy (Figure 5f).

These observations raised two questions. First, why did the latter sample show no anisotropy of the IF NMR enhancement factor? Actually, this apparent contradiction can be explained on simple geometrical considerations. While the c-axis of the *hcp* crystallites (easy magnetic axis) was preferentially oriented perpendicular to the wire axis, its azimuthal angle was evenly distributed because of the axial symmetry of the wires, as already observed by magnetic torque measurements.[27,67] As represented in the membrane top view of Figure 6b, even when the *rf* field was perpendicular to the wire axis, it could not coincide with all possible the orientations of the magnetic domains. As a result, the enhancement factor had an intermediate value between the one for a perpendicular and a parallel orientation. Due to angular symmetry, the overall enhancement factor can be approximated by:

$$\eta_{mean} = \frac{2}{\pi} * \int_0^{\frac{\pi}{2}} \eta(\theta) d\theta$$

with θ the angle between the domain orientation and the *rf* field. Approximations of the expression of the enhancement factor as function of θ, $\eta(\theta)$, have been proposed by Stearns et al.[69]. The power needed for an optimal excitation was therefore intermediate between the one needed for a perpendicular and a parallel orientation between the excitation field and the domain direction, observed for the samples with organic additives. Nevertheless, this reduced

enhancement factor for experiments with a *perpendicular* orientation still does not fully explain why it is the same as for experiments performed with a *parallel* orientation. In the case of a parallel orientation between the wire and *rf* field, the *rf* field would be perpendicular to all the domains normal to the wire axis, independently of their azimuthal angle, resulting in an even lower enhancement. An additional explanation is the fact that the wires were composed of a mixture of *hcp* and *fcc* Co crystalline structures, as deduced from the IF NMR spectrum (Figure 5c). Due to competition between the shape anisotropy and the perpendicular crystalline anisotropy (only from the *hcp* Co phases), the overall easy magnetic axis perpendicular to the wire was not very strong. This led to a situation with mixed domain orientations, where, besides their predominant perpendicular orientation, a significant part of the domains was also oriented alongside the wire axis.

Second, what is the origin of the different magnetic behaviors of the two samples of 200 nm Co nanowires grown in AAO membranes? This can be discussed in terms of competition between shape and magnetocrystalline anisotropy, as well as the effect of dipolar interactions. From geometrical considerations, the shape anisotropy was reduced and the dipolar interactions increased in the 200 nm samples compared to the 50 nm one. As a result, the magnetic easy axis was distributed more off axis, the coercivity, the remanence and the effective magnetic energy were reduced. As both samples had the same geometrical configuration, the different magnetic behavior must originate from a variation in their crystalline anisotropy. The XRD results (shown in Figure 3) suggested a first explanation: The sample grown in presence of additives appeared to be *fcc*-rich, resulting in a low crystalline anisotropy and a magnetic easy axis alongside the wire due to the effect of the shape anisotropy. The sample grown in absence of additives on the other hand, appeared to be *hcp*-rich with a *c*-axis perpendicular to the wire axis, leading to a strong

crystalline anisotropy and magnetic easy axis perpendicular to the wire. The analysis of the IF NMR spectra proposes an alternative explanation, however, as it shows an almost equal distribution of cobalt atoms between *fcc* and *hcp* crystallites for all the samples studied (Figure 5a-c). Nevertheless, a significant difference between the IF NMR spectra of the samples is that the ^{59}Co resonances of the 200 nm sample without additives were sharper, in particular with no extension towards the 210 MHz frequency range. Signal from such a low frequency range is generally attributed to grain boundaries, impurities or interfaces[61,65] From IF NMR this sample appeared thus more crystallized than the two others deposited with additives. When studying the deposition of cobalt thin films under similar conditions, it has been observed that the addition of organic additives, such as PEG, tends to inhibit the crystalline growth,[70,71] while in cobalt nanowires crystallite size is known to impact magnetic anisotropy and coercivity.[72,73] As a result, in our samples the size of the cobalt crystallites decreases, as reflected in the broader XRD and NMR peak width. In addition more grain boundaries are created and organic impurities from the additives, such as sulfur, tend to be incorporated inside the structure[71], explaining the additional NMR peak at lower frequencies. Besides differences in crystal symmetry (*fcc* or *hcp*), for the cobalt nanowires under consideration a crucial structural parameter to control magnetic anisotropy appeared to be differences in the crystallite size and grain boundaries.

5. CONCLUSIONS

Despite being easy to perform on a standard commercial solid-state NMR spectrometer, IF NMR is not a widespread method to characterize cobalt magnetic structures. While concerning the magnetic structure, magnetometry and IF NMR provided essentially the same information regarding anisotropy, concerning the crystalline structure, IF NMR nicely complemented XRD

characterization. Indeed, in our study of cobalt nanowires, it provided a more accurate picture of the distribution of *fcc* and *hcp* domains as well as of the presence and influence of defects at coherent domain boundaries. This allowed to better understand the influence of the presence of additives during the electrodeposition of cobalt on the magnetic properties of the formed nanowires. It was established that the organic additives determine the magnetic anisotropy of the nanowires more through the control of the grain boundaries than by modifying the *fcc* / *hcp* balance.

ASSOCIATED CONTENT

Supporting Information.

The following files are available free of charge. Supplementary XRD and IF NMR results, characterization of the 50 nm sample deposited in absence of polymer additives (PDF).

AUTHOR INFORMATION

Corresponding Author

Jean-Baptiste d'Espinose de Lacaillerie - SIMM, ESPCI Paris, Université PSL, CNRS UMR 7615, 10 Rue Vauquelin, 75005, Paris, France ; orcid.org/ 0000-0002-2463-6877 ;

Email: jean-baptiste.despinose@espci.fr

Present Addresses

† Alberto Quintana's present address - Institut de Ciència de Materials de Barcelona, Barcelona, Catalunya, Spain.

Author Contributions

The manuscript was written through contributions of all authors. All authors have given approval to the final version of the manuscript. IF NMR, XRD and SEM experiments were performed an analyzed by the ESPCI Paris team. Samples were synthesized by the GU team which also performed the magnetometry measurements.

ACKNOWLEDGMENT

NMR equipment at ESPCI Paris is funded in part by the Paris Region. This project has received funding from the European Union′s Horizon 2020 research and innovation program under the Marie Skłodowska-Curie grant agreement No 754387. Work at Georgetown University has been supported by the US NSF (ECCS-1933527). The acquisition of a Magnetic Property Measurements System (MPMS3) at GU, which was used in this investigation, was supported by the US-NSF (DMR-1828420). Bruno Bresson (ESPCI) is thanked for performing the SEM analysis.

REFERENCES

(1) Staňo, M.; Fruchart, O. Magnetic Nanowires and Nanotubes. In *Handbook of Magnetic Materials*; Elsevier, 2018; Vol. 27, pp 155–267. https://doi.org/10.1016/bs.hmm.2018.08.002.

(2) Vazquez, M. Cylindrical Nanowire Arrays: From Advanced Fabrication to Static and Microwave Magnetic Properties. *J. Magn. Magn. Mater.* **2022**, *543*, 168634. https://doi.org/10.1016/j.jmmm.2021.168634.

(3) Fert, A.; Piraux, L. Magnetic Nanowires. *J. Magn. Magn. Mater.* **1999**, *200* (1–3), 338–358. https://doi.org/10.1016/S0304-8853(99)00375-3.

(4) Blondel, A.; Meier, J. P.; Doudin, B.; Ansermet, J. -Ph. Giant Magnetoresistance of Nanowires of Multilayers. *Appl. Phys. Lett.* **1994**, *65* (23), 3019–3021. https://doi.org/10.1063/1.112495.

(5) Liu, K.; Nagodawithana, K.; Searson, P. C.; Chien, C. L. Perpendicular Giant Magnetoresistance of Multilayered Co/Cu Nanowires. *Phys. Rev. B* **1995**, *51* (11), 7381–7384. https://doi.org/10.1103/PhysRevB.51.7381.

(6) Maurice, J.-L.; Imhoff, D.; Etienne, P.; Durand, O.; Dubois, S.; Piraux, L.; George, J.-M.; Galtier, P.; Fert, A. Microstructure of Magnetic Metallic Superlattices Grown by Electrodeposition in Membrane Nanopores. *J. Magn. Magn. Mater.* **1998**, *184* (1), 1–18. https://doi.org/10.1016/S0304-8853(97)01104-9.

(7) Wong, J.; Greene, P.; Dumas, R. K.; Liu, K. Probing Magnetic Configurations in Co/Cu Multilayered Nanowires. *Appl. Phys. Lett.* **2009**, *94* (3), 032504. https://doi.org/10.1063/1.3073740.

(8) Berganza, E.; Marqués-Marchán, J.; Bran, C.; Vazquez, M.; Asenjo, A.; Jaafar, M. Evidence of Skyrmion-Tube Mediated Magnetization Reversal in Modulated Nanowires. *Materials* **2021**, *14* (19), 5671. https://doi.org/10.3390/ma14195671.

(9) Fernández-Pacheco, A.; Streubel, R.; Fruchart, O.; Hertel, R.; Fischer, P.; Cowburn, R. P. Three-Dimensional Nanomagnetism. *Nat. Commun.* **2017**, *8* (1), 15756. https://doi.org/10.1038/ncomms15756.

(10) Burks, E. C.; Gilbert, D. A.; Murray, P. D.; Flores, C.; Felter, T. E.; Charnvanichborikarn, S.; Kucheyev, S. O.; Colvin, J. D.; Yin, G.; Liu, K. 3D Nanomagnetism in Low Density Interconnected Nanowire Networks. *Nano Lett.* **2021**, *21* (1), 716–722. https://doi.org/10.1021/acs.nanolett.0c04366.

(11) Lee, S. A.; Yang, J. W.; Choi, S.; Jang, H. W. Nanoscale Electrodeposition: Dimension Control and 3D Conformality. *Exploration* **2021**, *1* (3), 20210012. https://doi.org/10.1002/EXP.20210012.

(12) Santhi, U.; Ngui, W. K.; Samykano, M.; Sudhakar, K.; Kadirgama, K.; Sangmesh, B.; Kumar, M. A. R. Cobalt Nanowires: Advancing into Future Nanomaterial. In *AIP Conference Proceedings*; Kuantan, Malaysia, 2019; p 020006. https://doi.org/10.1063/1.5085949.

(13) Déjardin, J.-L.; Franco, A.; Vernay, F.; Kachkachi, H. Ferromagnetic Resonance of a Two-Dimensional Array of Nanomagnets: Effects of Surface Anisotropy and Dipolar Interactions. *Phys. Rev. B* **2018**, *97* (22), 224407. https://doi.org/10.1103/PhysRevB.97.224407.

(14) Zhang, H.; Jia, W.; Sun, H.; Guo, L.; Sun, J. Growth Mechanism and Magnetic Properties of Co Nanowire Arrays by AC Electrodeposition. *J. Magn. Magn. Mater.* **2018**, *468*, 188–192. https://doi.org/10.1016/j.jmmm.2018.08.013.
(15) Das, B.; Mandal, K.; Sen, P.; Bakshi, A.; Das, P. Directional Change of Magnetic Easy Axis of Arrays of Cobalt Nanowires: Role of Non-Dipolar Magnetostatic Interaction. *Phys. B Condens. Matter* **2012**, *407* (18), 3767–3773. https://doi.org/10.1016/j.physb.2012.05.058.
(16) Chen, W.-H.; Cheng, H.-C.; Hsu, Y.-C.; Uang, R.-H.; Hsu, J.-S. Mechanical Material Characterization of Co Nanowires and Their Nanocomposite. *Compos. Sci. Technol.* **2008**, *68* (15–16), 3388–3395. https://doi.org/10.1016/j.compscitech.2008.09.030.
(17) Hayashi, M.; Thomas, L.; Rettner, C.; Moriya, R.; Parkin, S. S. P. Real Time Observation of the Field Driven Periodic Transformation of Domain Walls in Permalloy Nanowires at the Larmor Frequency and Its First Harmonic. *Appl. Phys. Lett.* **2008**, *92* (11), 112510. https://doi.org/10.1063/1.2890036.
(18) Parkin, S. S. P.; Hayashi, M.; Thomas, L. Magnetic Domain-Wall Racetrack Memory. *Science* **2008**, *320* (5873), 190. https://doi.org/10.1126/science.1145799.
(19) Herrera Diez, L.; Liu, Y. T.; Gilbert, D. A.; Belmeguenai, M.; Vogel, J.; Pizzini, S.; Martinez, E.; Lamperti, A.; Mohammedi, J. B.; Laborieux, A.; Roussigné, Y.; Grutter, A. J.; Arenholtz, E.; Quarterman, P.; Maranville, B.; Ono, S.; Hadri, M. S. E.; Tolley, R.; Fullerton, E. E.; Sanchez-Tejerina, L.; Stashkevich, A.; Chérif, S. M.; Kent, A. D.; Querlioz, D.; Langer, J.; Ocker, B.; Ravelosona, D. Nonvolatile Ionic Modification of the Dzyaloshinskii-Moriya Interaction. *Phys. Rev. Appl.* **2019**, *12* (3), 034005. https://doi.org/10.1103/PhysRevApplied.12.034005.
(20) Parkin, S.; Yang, S.-H. Memory on the Racetrack. *Nat. Nanotechnol.* **2015**, *10* (3), 195–198. https://doi.org/10.1038/nnano.2015.41.
(21) Kac, M.; Zarzycki, A.; Kac, S.; Kopec, M.; Perzanowski, M.; Dutkiewicz, E. M.; Suchanek, K.; Maximenko, A.; Marszalek, M. Effect of the Template-Assisted Electrodeposition Parameters on the Structure and Magnetic Properties of Co Nanowire Arrays. *Mater. Sci. Eng. B* **2016**, *211*, 75–84. https://doi.org/10.1016/j.mseb.2016.06.004.
(22) Caffarena, V. R.; Guimarães, A. P.; Folly, W. S. D.; Silva, E. M.; Capitaneo, J. L. Magnetic Behavior of Electrodeposited Cobalt Nanowires Using Different Electrolytic Bath Acidities. *Mater. Chem. Phys.* **2008**, *107* (2–3), 297–304. https://doi.org/10.1016/j.matchemphys.2007.07.016.
(23) Ferré, R.; Ounadjela, K.; George, J. M.; Piraux, L.; Dubois, S. Magnetization Processes in Nickel and Cobalt Electrodeposited Nanowires. *Phys. Rev. B* **1997**, *56* (21), 14066–14075. https://doi.org/10.1103/PhysRevB.56.14066.
(24) Wegrowe, J.-E.; Kelly, D.; Franck, A.; Gilbert, S. E.; Ansermet, J.-Ph. Magnetoresistance of Ferromagnetic Nanowires. *Phys. Rev. Lett.* **1999**, *82* (18), 3681–3684. https://doi.org/10.1103/PhysRevLett.82.3681.
(25) Piraux, L.; Dubois, S.; Ferain, E.; Legras, R.; Ounadjela, K.; George, J. M.; Maurice, J. L.; Fert, A. Anisotropic Transport and Magnetic Properties of Arrays of Sub-Micron Wires. *J. Magn. Magn. Mater.* **1997**, *165* (1–3), 352–355. https://doi.org/10.1016/S0304-8853(96)00553-7.
(26) Wernsdorfer, W.; Doudin, B.; Mailly, D.; Hasselbach, K.; Benoit, A.; Meier, J.; Ansermet, J.-Ph.; Barbara, B. Nucleation of Magnetization Reversal in Individual Nanosized Nickel

Wires. *Phys. Rev. Lett.* **1996**, *77* (9), 1873–1876. https://doi.org/10.1103/PhysRevLett.77.1873.
(27) Henry, Y.; Ounadjela, K.; Piraux, L.; Dubois, S.; George, J.-M.; Duvail, J.-L. Magnetic Anisotropy and Domain Patterns in Electrodeposited Cobalt Nanowires. *Eur. Phys. J. B* **2001**, *20* (1), 35–54. https://doi.org/10.1007/s100510170283.
(28) Chen, G.; Mascaraque, A.; Jia, H.; Zimmermann, B.; Robertson, M.; Conte, R. L.; Hoffmann, M.; González Barrio, M. A.; Ding, H.; Wiesendanger, R.; Michel, E. G.; Blügel, S.; Schmid, A. K.; Liu, K. Large Dzyaloshinskii-Moriya Interaction Induced by Chemisorbed Oxygen on a Ferromagnet Surface. *Sci. Adv.* **2020**, *6* (33), eaba4924. https://doi.org/10.1126/sciadv.aba4924.
(29) Chen, G.; Robertson, M.; Hoffmann, M.; Ophus, C.; Fernandes Cauduro, A. L.; Lo Conte, R.; Ding, H.; Wiesendanger, R.; Blügel, S.; Schmid, A. K.; Liu, K. Observation of Hydrogen-Induced Dzyaloshinskii-Moriya Interaction and Reversible Switching of Magnetic Chirality. *Phys. Rev. X* **2021**, *11* (2), 021015. https://doi.org/10.1103/PhysRevX.11.021015.
(30) Gossard, A. C.; Portis, A. M. Observation of Nuclear Resonance in a Ferromagnet. *Phys. Rev. Lett.* **1959**, *3* (4), 164–166. https://doi.org/10.1103/PhysRevLett.3.164.
(31) Liu, Y.; Luo, J.; Shin, Y.; Moldovan, S.; Ersen, O.; Hébraud, A.; Schlatter, G.; Pham-Huu, C.; Meny, C. Sampling the Structure and Chemical Order in Assemblies of Ferromagnetic Nanoparticles by Nuclear Magnetic Resonance. *Nat. Commun.* **2016**, *7*, 11532. https://doi.org/10.1038/ncomms11532.
(32) Andreev, A. S.; d'Espinose de Lacaillerie, J.-B.; Lapina, O. B.; Gerashenko, A. Thermal Stability and Hcp–Fcc Allotropic Transformation in Supported Co Metal Catalysts Probed near Operando by Ferromagnetic NMR. *Phys. Chem. Chem. Phys.* **2015**, *17* (22), 14598–14604. https://doi.org/10.1039/C4CP05327C.
(33) Yakovlev, I. V.; Yakushkin, S. S.; Kazakova, M. A.; Trukhan, S. N.; Volkova, Z. N.; Gerashchenko, A. P.; Andreev, A. S.; Ishchenko, A. V.; Martyanov, O. N.; Lapina, O. B.; d'Espinose de Lacaillerie, J.-B. Superparamagnetic Behaviour of Metallic Co Nanoparticles According to Variable Temperature Magnetic Resonance. *Phys. Chem. Chem. Phys.* **2021**, *23* (4), 2723–2730. https://doi.org/10.1039/D0CP05963C.
(34) Strijkers, G. J.; Dalderop, J. H. J.; Broeksteeg, M. A. A.; Swagten, H. J. M.; de Jonge, W. J. M. Structure and Magnetization of Arrays of Electrodeposited Co Wires in Anodic Alumina. *J. Appl. Phys.* **1999**, *86* (9), 5141–5145. https://doi.org/10.1063/1.371490.
(35) De Riedmatten, H.; Scarani, V.; Ansermet, J.-P. Effect of Oxidation of Cobalt-Based Nanowires on NMR Spin-Lattice Relaxation. *Appl. Magn. Reson.* **2000**, *19* (3–4), 439–445. https://doi.org/10.1007/BF03162387.
(36) Scarani, V.; De Riedmatten, H.; Ansermet, J.-P. 59Co Nuclear Magnetic Resonance Studies of Magnetic Excitations in Ferromagnetic Nanowires. *Appl. Phys. Lett.* **2000**, *76* (7), 903–905. https://doi.org/10.1063/1.125624.
(37) Scarani, V.; Doudin, B.; Ansermet, J.-P. The Microstructure of Electrodeposited Cobalt-Based Nanowires and Its Effect on Their Magnetic and Transport Properties. *J. Magn. Magn. Mater.* **1999**, *205* (2–3), 8. https://doi.org/10.1016/S0304-8853(99)00513-2.
(38) Doudin, B.; Wegrowe, J. E.; Gilbert, S. E.; Scarani, V.; Kelly, D.; Meier, J. P.; Ansermet, J.-P. Magnetic and Transport Properties of Electrodeposited Nanostructured Nanowires. *IEEE Trans. Magn.* **1998**, *34* (4), 968–972. https://doi.org/10.1109/20.706328.

(39) Gilbert, D. A.; Burks, E. C.; Ushakov, S. V.; Abellan, P.; Arslan, I.; Felter, T. E.; Navrotsky, A.; Liu, K. Tunable Low Density Palladium Nanowire Foams. *Chem. Mater.* **2017**, *29* (22), 9814–9818. https://doi.org/10.1021/acs.chemmater.7b03978.
(40) Malloy, J.; Quintana, A.; Jensen, C. J.; Liu, K. Efficient and Robust Metallic Nanowire Foams for Deep Submicrometer Particulate Filtration. *Nano Lett.* **2021**, *21* (7), 2968–2974. https://doi.org/10.1021/acs.nanolett.1c00050.
(41) Vicenzo, A.; Cavallotti, P. L. Growth Modes of Electrodeposited Cobalt. *Electrochimica Acta* **2004**, *49* (24), 4079–4089. https://doi.org/10.1016/j.electacta.2004.04.001.
(42) Watts, O. P. Rapid Nickel Plating. *Trans. Am. Electrochem. Soc* **1916**, *29*, 395–403.
(43) Guimarães, A. P. *Magnetism and Magnetic Resonance in Solids*; John Wiley & Sons: New York, 1998.
(44) Turov, E. A.; Petrov, M. P. *Nuclear Magnetic Resonance in Ferro- and Antiferromagnets*; Israel Program for scientific translations (Halsted Press): Jerusalem, 1972.
(45) Massiot, D.; Fayon, F.; Capron, M.; King, I.; Le Calvé, S.; Alonso, B.; Durand, J.-O.; Bujoli, B.; Gan, Z.; Hoatson, G. Modelling One- and Two-Dimensional Solid-State NMR Spectra: Modelling 1D and 2D Solid-State NMR Spectra. *Magn. Reson. Chem.* **2002**, *40* (1), 70–76. https://doi.org/10.1002/mrc.984.
(46) Armyanov, S. Crystallographic Structure and Magnetic Properties of Electrodeposited Cobalt and Cobalt Alloys. *Electrochimica Acta* **2000**, *45* (20), 3323–3335. https://doi.org/10.1016/S0013-4686(00)00408-4.
(47) Santos, J. S.; Matos, R.; Trivinho-Strixino, F.; Pereira, E. C. Effect of Temperature on Co Electrodeposition in the Presence of Boric Acid. *Electrochimica Acta* **2007**, *53* (2), 644–649. https://doi.org/10.1016/j.electacta.2007.07.025.
(48) Rigsby, M. A.; Spurlin, T. A.; Reid, J. D. The Multi-Functional Role of Boric Acid in Cobalt Electrodeposition and Superfill. *J. Electrochem. Soc.* **2020**, *167* (11), 112507. https://doi.org/10.1149/1945-7111/aba640.
(49) Whitney, T. M.; Searson, P. C.; Jiang, J. S.; Chien, C. L. Fabrication and Magnetic Properties of Arrays of Metallic Nanowires. *Science* **1993**, *261* (5126), 1316–1319. https://doi.org/10.1126/science.261.5126.1316.
(50) Rahman, M. T.; Dumas, R. K.; Eibagi, N.; Shams, N. N.; Wu, Y.-C.; Liu, K.; Lai, C.-H. Controlling Magnetization Reversal in Co/Pt Nanostructures with Perpendicular Anisotropy. *Appl. Phys. Lett.* **2009**, *94* (4), 042507. https://doi.org/10.1063/1.3075061.
(51) Liu, K.; Chien, C. L. Magnetic and Magneto-Transport Properties of Novel Nanostructured Networks. *IEEE Trans. Magn.* **1998**, *34* (4), 1021–1023. https://doi.org/10.1109/20.706344.
(52) Saeki, R.; Ohgai, T. Determination of Activation Overpotential during the Nucleation of Hcp-Cobalt Nanowires Synthesized by Potentio-Static Electrochemical Reduction. *Materials* **2018**, *11* (12), 2355. https://doi.org/10.3390/ma11122355.
(53) Chien, C. L. Granular Magnetic Solids (Invited). *J. Appl. Phys.* **1991**, *69* (8), 5267–5272. https://doi.org/10.1063/1.348946.
(54) Kou, X.; Fan, X.; Dumas, R. K.; Lu, Q.; Zhang, Y.; Zhu, H.; Zhang, X.; Liu, K.; Xiao, J. Q. Memory Effect in Magnetic Nanowire Arrays. *Adv. Mater.* **2011**, *23* (11), 1393–1397. https://doi.org/10.1002/adma.201003749.
(55) Zamani Kouhpanji, M. R.; Ghoreyshi, A.; Visscher, P. B.; Stadler, B. J. H. Facile Decoding of Quantitative Signatures from Magnetic Nanowire Arrays. *Sci. Rep.* **2020**, *10* (1), 15482. https://doi.org/10.1038/s41598-020-72094-4.

(56) Chen, F.; Wang, F.; Jia, F.; Li, J.; Liu, K.; Huang, S.; Luan, Z.; Wu, D.; Chen, Y.; Zhu, J.; Peng, R.-W.; Wang, M. Periodic Magnetic Domains in Single-Crystalline Cobalt Filament Arrays. *Phys. Rev. B* **2016**, *93* (5), 054405. https://doi.org/10.1103/PhysRevB.93.054405.
(57) Liu, Z.; Chang, P.-C.; Chang, C.-C.; Galaktionov, E.; Bergmann, G.; Lu, J. G. Shape Anisotropy and Magnetization Modulation in Hexagonal Cobalt Nanowires: Magnetization Modulation in Cobalt Nanowires. *Adv. Funct. Mater.* **2008**, *18* (10), 1573–1578. https://doi.org/10.1002/adfm.200701010.
(58) Gossard, A. C.; Portis, A. M.; Rubinstein, M.; Lindquist, R. H. Ferromagnetic Nuclear Resonance of Single-Domain Cobalt Particles. *Phys. Rev.* **1965**, *138* (5A), A1415–A1421. https://doi.org/10.1103/PhysRev.138.A1415.
(59) Osborn, J. A. Demagnetizing Factors of the General Ellipsoid. *Phys. Rev.* **1945**, *67* (11–12), 351–357. https://doi.org/10.1103/PhysRev.67.351.
(60) Panissod, P. Structural and Magnetic Investigations of Ferromagnets by NMR. Application to Magnetic Metallic Multilayers. In *Frontiers in Magnetism of Reduced Dimension Systems*; Bar'yakthar, V. G., Wigen, P. E., Lesnik, N. A., Eds.; Springer Netherlands: Dordrecht, 1998; pp 225–270. https://doi.org/10.1007/978-94-011-5004-0_10.
(61) Sort, J.; Suriñach, S.; Muñoz, J. S.; Baró, M. D.; Wojcik, M.; Jedryka, E.; Nadolski, S.; Sheludko, N.; Nogués, J. Role of Stacking Faults in the Structural and Magnetic Properties of Ball-Milled Cobalt. *Phys. Rev. B* **2003**, *68* (1). https://doi.org/10.1103/PhysRevB.68.014421.
(62) Andreev, A. S.; Lapina, O. B.; Cherepanova, S. V. A New Insight into Cobalt Metal Powder Internal Field 59Co NMR Spectra. *Appl. Magn. Reson.* **2014**, *45* (10), 1009–1017. https://doi.org/10.1007/s00723-014-0580-0.
(63) Matveev, V. V.; Baranov, D. A.; Yurkov, G. Yu.; Akatiev, N. G.; Dotsenko, I. P.; Gubin, S. P. Cobalt Nanoparticles with Preferential Hcp Structure: A Confirmation by X-Ray Diffraction and NMR. *Chem. Phys. Lett.* **2006**, *422* (4–6), 402–405. https://doi.org/10.1016/j.cplett.2006.02.099.
(64) *Frontiers in Magnetism of Reduced Dimension Systems*; Bar'yakthar, V. G., Wigen, P. E., Lesnik, N. A., Eds.; Springer Netherlands: Dordrecht, 1998. https://doi.org/10.1007/978-94-011-5004-0.
(65) Cadeville, M. C.; Deportes, J. Saturation Magnetizations and High Field Susceptibilities of C and C Interstitial Solid Solutions. *Phys. Lett. A* **1972**, *41* (3), 237–238. https://doi.org/10.1016/0375-9601(72)90275-7.
(66) Johnson, M. T.; Bloemen, P. J. H.; Broeder, F. J. A. den; Vries, J. J. de. Magnetic Anisotropy in Metallic Multilayers. *Rep. Prog. Phys.* **1996**, *59* (11), 1409–1458. https://doi.org/10.1088/0034-4885/59/11/002.
(67) Ounadjela, K.; Ferré, R.; Louail, L.; George, J. M.; Maurice, J. L.; Piraux, L.; Dubois, S. Magnetization Reversal in Cobalt and Nickel Electrodeposited Nanowires. *J. Appl. Phys.* **1997**, *81* (8), 5455–5457. https://doi.org/10.1063/1.364568.
(68) Prejbeanu, I. L.; Buda, L. D.; Ebels, U.; Viret, M.; Fermon, C.; Ounadjela, K. Domain Structures in Epitaxial (1010) Co Wires. *IEEE Trans. Magn.* **2001**, *37* (4), 2108–2110. https://doi.org/10.1109/20.951068.
(69) Stearns, M. B. Spin-Echo and Free-Induction-Decay Measurements in Pure Fe and Fe-Rich Ferromagnetic Alloys: Domain-Wall Dynamics. *Phys. Rev.* **1967**, *162* (2), 496–509. https://doi.org/10.1103/PhysRev.162.496.

(70) Ni, X.; Chen, Y.; Jin, X.; Wang, C.; Huang, Y.; Hong, Y.; Su, X.; Zhou, G.; Wang, S.; He, W.; Chen, Q. Investigation of Polyvinylpyrrolidone as an Inhibitor for Trench Super-Filling of Cobalt Electrodeposition. *J. Taiwan Inst. Chem. Eng.* **2020**, *112*, 232–239. https://doi.org/10.1016/j.jtice.2020.06.010.
(71) Hu, Y.; Deb, S.; Li, D.; Huang, Q. Effects of Organic Additives on the Impurity and Grain Structure of Electrodeposited Cobalt. *Electrochimica Acta* **2021**, *368*, 137594. https://doi.org/10.1016/j.electacta.2020.137594.
(72) Saini, D.; Chauhan, R. P.; Kumar, S. Effects of Annealing on Structural and Magnetic Properties of Template Synthesized Cobalt Nanowires Useful as Data Storage and Nano Devices. *J. Mater. Sci. Mater. Electron.* **2014**, *25* (1), 124–127. https://doi.org/10.1007/s10854-013-1560-0.
(73) Maaz, K.; Karim, S.; Usman, M.; Mumtaz, A.; Liu, J.; Duan, J. L.; Maqbool, M. Effect of Crystallographic Texture on Magnetic Characteristics of Cobalt Nanowires. *Nanoscale Res. Lett.* **2010**, *5* (7), 1111–1117. https://doi.org/10.1007/s11671-010-9610-5.

Supporting information

Magnetic structure and internal field nuclear magnetic resonance in cobalt nanowires

Pascal Scholzen,[1] Guillaume Lang,[2] Andrey S. Andreev,[3] Alberto Quintana,[4] James Malloy,[4] Christopher J. Jensen,[4] Kai Liu,[4] and Jean-Baptiste d'Espinose de Lacaillerie[1]**

(1) SIMM, ESPCI Paris, Université PSL, CNRS UMR 7615, 10 Rue Vauquelin, 75005, Paris, France.

(2) LPEM, ESPCI Paris, Université PSL, CNRS UMR 8213, 10 Rue Vauquelin, 75005, Paris, France.

(3) TotalEnergies One Tech Belgium (TEOTB), Zone Industrielle C, 7181 Feluy, Belgium

(4) Physics Department, Georgetown University, Washington, DC 20057, USA

KEYWORDS. ^{59}Co NMR, internal field NMR, ferromagnetism, metallic nanostructures, nanomagnetism, FNR.

Scherrer analysis for particle size and lattice parameters

In order to perform the Scherrer analysis, the different peaks of the diffractograms in Figure 3 were fitted with a Pseudo-Voigt line shape and considering the $K_{\alpha,1}$ and $K_{\alpha,2}$ contributions. The size (D) of the crystallites is then determined using Scherrer's formula:[1]

$$D = \frac{K\lambda}{\beta\, cos\theta}$$

with K the form/Scherrer factor (set equal to 0.9, because unknown crystallite shape), λ the wavelength (Cu anode => 0.15406 nm), β the FWHM of the Pseudo-Voigt peak (2θ in rad, after subtraction of the machine contribution: 0.08°) and θ the Bragg angle (in rad).

Table S1. Crystallite size estimates obtained from the XRD diffraction peaks for the different samples analyzed in this work.

		200 nm with additives		200 nm no additives	
Angle 2θ (°)	Diffraction planes	FWHM (°)	Crystallite size (nm)	FWHM (°)	Crystallite size (nm)
41.6	*hcp* (100)	/	/	0.44	23.6
44.3	*hcp* (002)/ *fcc* (111)	1.05	8.8	0.91	10.3
51.5	*fcc* (200)	1.9	4.8	/	
75.9	*hcp* (110)/ *fcc* (220)	1.5	7.1	0.66	17.2
92.4	*hcp* (112)/ *fcc* (311)	1.6	7.5	1.2	10.2

The lattice parameters of the cubic fcc phase in the 200 nm samples can be calculated using the formula:

$$\frac{1}{d^2} = \frac{h^2 + l^2 + k^2}{a^2}$$

With d^2 the interplanar spacing of and h, l, k the Miller indices of the diffraction plane and a the lattice parameter of the fcc structure. This formula can be applied to each peak and an average lattice parameter is calculated.

The determination of the lattice parameters of the hexagonal phase is more complicated. There exist two lattice parameters: c defining the vertical dimension and a defining the hexagonal base (considered to be equilateral). The parameter c can be determined from the position of the *hcp* (002) peak, while the position of the *hcp* (100) and *hcp* (110) peaks can be used in order to determine the parameter a.

It has to be noted that the precision of the lattice parameter calculation is limited, due to the low

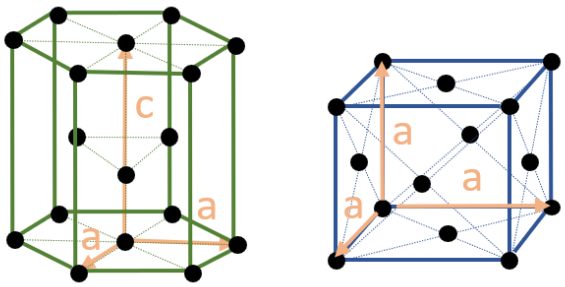

hcp *fcc*

signal intensity and the overlapping of *fcc/hcp* peaks. As a result, the exact peak positions cannot be determined very precisely.

Table S2. Lattice parameters estimates from the XRD diffraction peaks for the different samples analyzed in this work.

		200 nm with additives		200 nm no additives	
Angle 2θ (°)	Diffraction planes	*fcc* lattice parameter (Å)	*hcp* lattice parameter (Å)	*fcc* lattice parameter (Å)	*hcp* lattice parameter (Å)
41.6	*hcp* (100)	/	/	/	a = 2.5
44.3	*hcp* (002)/ *fcc* (111)	a = 3.55	c = 4.1	a = 3.55	c = 4.1
51.5	*fcc* (200)	a = 3.58	/	/	/
75.9	*hcp* (110)/ *fcc* (220)	a = 3.56	a = 2.5	a = 3.56	a = 2.5
92.4	*hcp* (112)/ *fcc* (311)	a = 3.55	/	a = 3.55	/
		Average: $a = 3.56$		Average: $a = 3.55$	

Supplementary characterization of the 50 nm sample with additives

The following X-ray diffraction (XRD) pattern comes from the analysis of Co nanowires grown in the 50 nm pores of a PC membrane, in presence of organic additives in the electrolyte. The precise synthesis conditions, as well as more details about the XRD experiments are presented in the main paper. As highlighted in the graph, the only four peaks that can be distinguished (44.5°, 64.5°, 77.5°, 81.9°) correspond to signal from the gold (Au) electrode attached to the bottom of the membrane, probably covering peaks corresponding to signal from *fcc*/*hcp* cobalt. No determination of the Co crystalline phase was therefore possible.

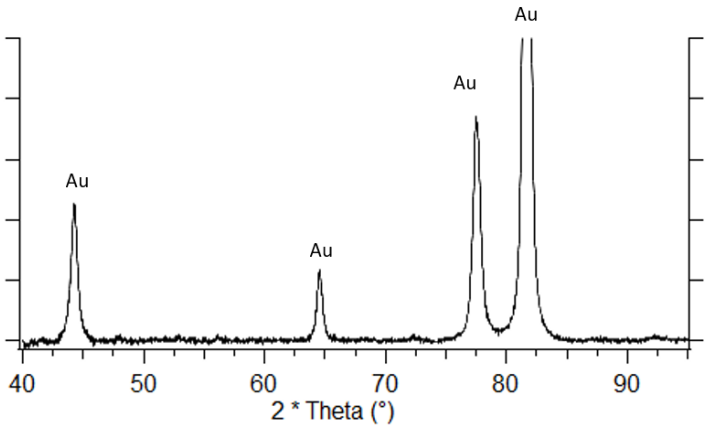

Figure S1. XRD pattern collected on 50 nm Co nanowires grown in the pores of a PC membrane in presence of organic additives in the electrolyte. The samples are analyzed with the membrane plane being in the XRD diffraction plane (*i.e.* the wire axis normal to the diffraction plane).

Supplementary characterization of the 50 nm without additives

The following results were obtained from wires grown into the 50 nm pores of a PC membrane, in absence of organic additives in the electrolyte. The characteristics of the membrane were the same as of the one used for the production of 50 nm nanowires deposited in presence of organic additives and are described in the main article. The composition of the electrolyte was the same as the one of the 200 nm nanowires without additives, namely: 240 g/L $CoSO_4 \cdot 7H_2O$ + 50 g/L $CoCl_2 \cdot 6H_2O$ + 40 g/L H_3BO_3.

XRD. The XRD pattern of this sample is shown in Figure S2.

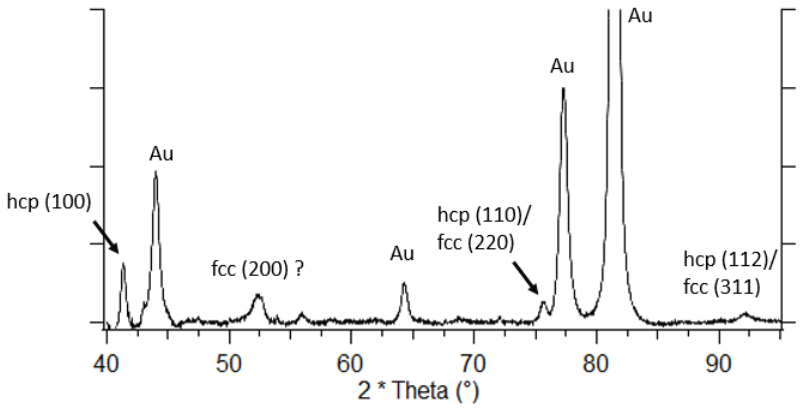

Figure S2. a XRD pattern collected on 50 nm Co nanowires grown in the pores of a PC membrane in absence of organic additives in the electrolyte. The samples are analyzed with the membrane plane being in the XRD diffraction plane.

Besides the 4 peaks corresponding to signal form the Au electrode still attached to the membrane, 3 peaks assigned to cobalt clearly can be distinguished: 41.5° (*hcp* (100), 75.9° (*hcp*

(110)/ *fcc* (220)) and 92.3° (*hcp* (112)/ *fcc* (311)). The two peaks around 52.5° and 56.0° cannot be assigned to neither Co, nor Au structures, even though the former one is close to the characteristic peak of *fcc* Co (200) around 51.5°. Due to the strong Au signal around 44.5°, peaks corresponding to *hcp* (002)/ *fcc* (111) cobalt might be covered, which makes it difficult to analyze the crystalline structure by XRD. Nevertheless, the relatively strong *hcp* (100) Co peak indicates that a significant part of the sample had a hexagonal crystalline structure with its *c*-axis perpendicular to the wire axis.

Magnetic hysteresis measurement. The magnetic properties of the 50 nm Co nanowires deposited in absence of organic additives were studied at room temperature with a magnetic field applied perpendicularly (⊥) or parallel (||) to the wire axis, as shown in **Figure S3**.

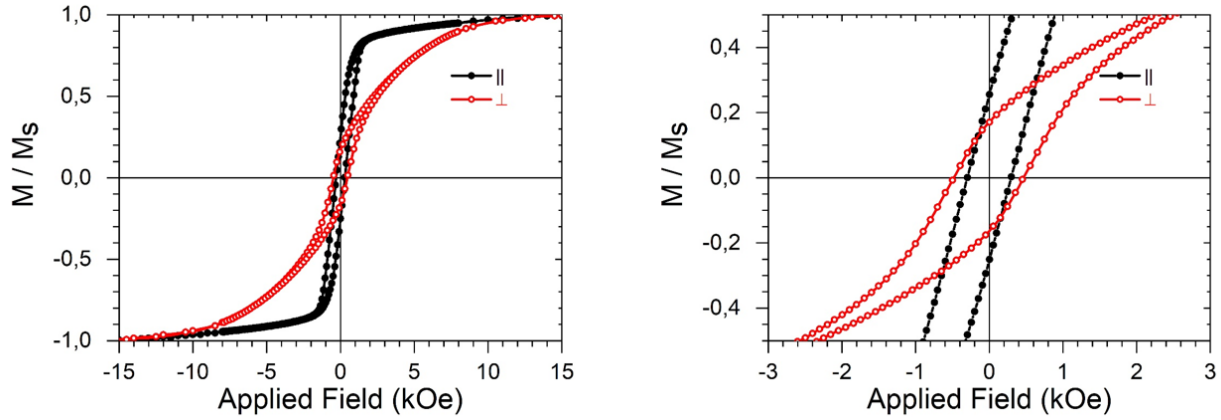

Figure S3. Magnetic hysteresis loops recorded on 50 nm Co nanowires grown in the pores of a PC membrane in absence of organic additives. The measurements were performed at ambient temperature with the field applied perpendicular (⊥, red hollow symbols) or parallel (||, black full symbols) to the cobalt wires. Left: full loops. Right: Zoom-in view of the full loops.

The loops are fairly similar to the ones observed on 50 nm Co nanowires deposited in presence of organic additives, shown in **Figure 4** a). Squared hysteresis loops with a coercivity of about

500 Oe measured on-axis (i.e. parallel) can be seen, as well as a clear magnetic easy axis parallel to the nanowires.

In Figure S4, the internal field (IF) NMR analysis in the frequency range associated with ^{59}Co resonances obtained from 50 nm nanowires without additives is represented. The spectrum (left) is mainly composed of two peaks, corresponding to cobalt in *fcc* multi-domain and *hcp* structures. In addition, a small peak around 216 MHz can be distinguished, which could be assigned to *fcc* stacking faults or *fcc* structures with a residual demagnetization field. The amount of *hcp* Co detected by NMR was significantly bigger than the amount of *fcc*, which differentiated this samples from all the other ones analyzed, where both phases were present in more or less the same quantity (**Figure S5**). The narrow peak width and the absence of a significant signal below 210 MHz (especially compared to the samples grown in presence of additives) suggest that cobalt was well crystallized, with big crystalline domains and few grain boundaries/ impurities. As the signal around 213 MHz can unambiguously be assigned to signal from fcc multi-domain structures and the optimal power is pretty much flat over the whole frequency range, it can be concluded that a major part of the signal arose from multi-domain structures and therefore the excitation of domain walls. The power needed for an optimal excitation and consequently also the enhancement factor is anisotropic, with less power needed for a parallel orientation between the *rf* field and the wire axis. This was the result a multi-domain structure and an easy axis of magnetization colinear with the wire, as confirmed by the magnetic hysteresis measurements (**Figure S3**). It could be concluded that the strong shape anisotropy of the 50 nm wires results was dominant over the *hcp* Co crystalline anisotropy (dipolar interactions could be neglected due to the big interwire distance), in contrast to the 200 nm sample synthesized under the same conditions. The NMR results showed the presence of a big amount of *hcp* Co in the sample but

gave no information about the orientation of its *c*-axis (easy axis of magnetization). The XRD analysis with the membrane plane in the diffraction plane, shown in Figure S2, suggested that a significant part of the sample had a hexagonal crystalline structure with its *c*-axis perpendicular to the wire axis. However, the presence of the gold electrode at the bottom of the membrane made it difficult to obtain more information by XRD.

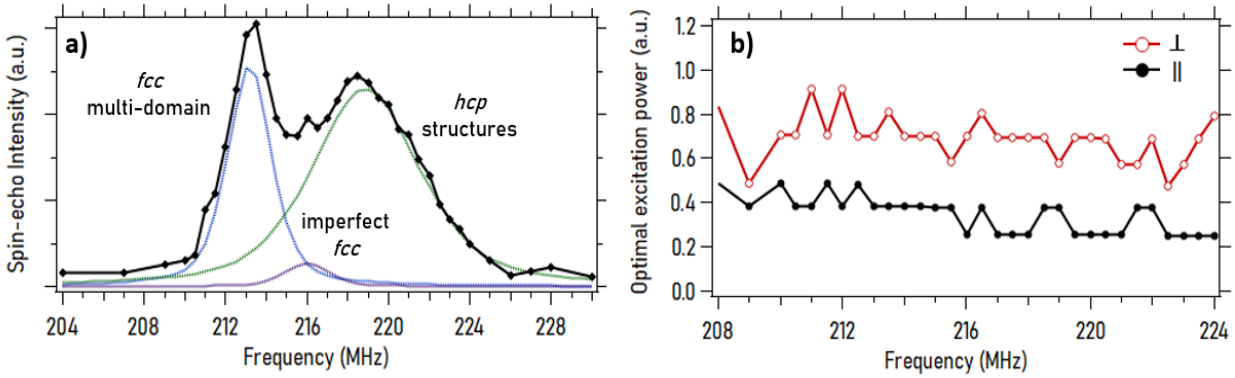

Figure S4. a) ^{59}Co IF NMR room temperature spectrum of 50 nm Co nanowires grown in PC membrane in absence of organic additives in the electrolyte. A tentative decomposition into peaks corresponding to different crystalline and magnetic structures is also presented, with the relative amounts of the different phases given in **Figure S5**. The spectral shape is identical regardless of the orientation between the *rf* pulse and the wire axis, so only one orientation is represented here. The graphs b) corresponds to the optimal excitation power for the same sample for different orientations: The red line (hollow spheres) corresponds to a perpendicular (⊥) orientation between the direction of the *rf* pulse and the wire axis, the black line (full spheres) to a parallel (||) one.

Overview of the measured relaxation times

The T_2 (spin-spin) relaxation time has been measured at three frequencies (213.5 MHz, 215.5 MHz and 218 MHz) for all the samples. The measured values for the different spectra represented in Figure 5 and Figure S4 are represented in Table S3. It can be seen that the T_2 relaxation time for the *fcc* Co multi-domain peak (213.5 MHz) is about 20-21 µs, while it is about 24-25 µs for the *hcp* Co peak (218 MHz). The value measured at 215.5 MHz (assigned to imperfect *fcc* Co) is generally in between those values. For a constant intensity of the *fcc* Co multi-domain peak, this leads to an about 5-15 % lower signal intensity after T_2 correction of the two other peaks.

In the literature, the T_2 values of different Co crystalline structures are not distinguished (it is generally given to be around 20-25 µs)[2]. As a result, it is difficult to use the T_2 data to assign help with the decomposition of the spectrum. Nevertheless, it was observed that the T_2 relaxation time is systematically the shortest for the *fcc* Co multi-domain phase, compared to the other ones.

Table S3. T_2 relaxation times measured for the different samples analyzed in this work.

	Additifs		No Additifs	
Frequency (MHz)	50 nm	200 nm	200 nm	50 nm
213.5	21 µs	21 µs	20 µs	21 µs
215.5	22 µs	23 µs	25 µs	25 µs
218	24 µs	24 µs	24 µs	25 µs

The T_1 (spin-lattice) relaxation time has also been measured for some samples using an saturation-recovery pulse sequence and values between 325 µs and 500 µs have been obtained,

which is in accordance with results obtained in the literature.[3] This justifies the short repetition rate (67 Hz) and shows that corrections of the spectrum intensity for this relaxation time are unsignificant.

Overview of the relative signal intensity of the different phases for the analyzed samples

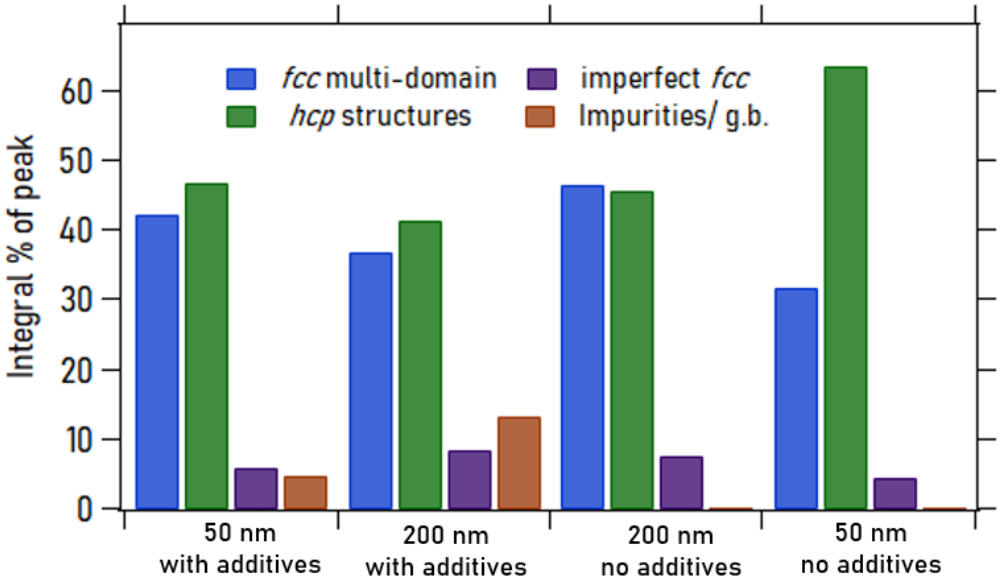

Figure S5. Quantitative distribution of the different crystalline/ magnetic phases detected by ^{59}Co IF NMR for the samples presented in this work. The corresponding spectra are shown in Figure 5 and Figure S4.

Fitting overview

The fitting of all the spectra has been performed using the DMFIT program and the detailed fitting parameters can be found in Table S4. For the samples synthesized in absence of additives in the electrolyte, the spectra can be fitted well with three peaks. In addition, only the position and width of the smallest peak were fixed in order to obtain the best fit.

For the samples synthesized in presence of additives in the electrolyte an additional peak needs to be added in order to account for grain-boundaries and impurities. Due to this additional peak,

the number of degrees of freedom had to be reduced in order to obtain a stable fitting (only the exact position of the 213 MHz peak and the intensity of all peaks were allowed to vary). However, the different peak positions and widths have been optimized manually.

Table S4. Fit parameters for the peaks of the decomposition of the ^{59}Co IF NMR spectra obtained from the different samples analyzed in this work. The star (*) behind a parameter signifies that this parameter was allowed to vary during the fitting procedure. The Gaussian/Lorentzian rate of the peak line shape was set to 0.5 for all peaks.

	Position (MHz)	Width (MHz)	Rel. Intensity (%)
50 nm PC additives	213.3*	3.0	42*
	218.5	5.6	47*
	215.5	2.5	6*
	210.0	3.5	5*
200 nm AAO additives	213.2*	3.0	37*
	218.5	5.6	41*
	216.0	2.5	9*
	210.0	3.5	13*
200 nm AAO no additives	213.3*	2.4*	47*
	218.9*	5.7*	46*
	216.0	2.5	8*
50 nm PC no additives	213.3*	2.4*	32*
	219.0*	6.1*	64*
	216.0	2.5	5*

References

(1) Holder, C. F.; Schaak, R. E. Tutorial on Powder X-Ray Diffraction for Characterizing Nanoscale Materials. *ACS Nano* **2019**, *13* (7), 7359–7365. https://doi.org/10.1021/acsnano.9b05157.

(2) Scarani, V.; Doudin, B.; Ansermet, J.-P. The Microstructure of Electrodeposited Cobalt-Based Nanowires and Its Effect on Their Magnetic and Transport Properties. *J. Magn. Magn. Mater.* **1999**, *205* (2–3), 8. https://doi.org/10.1016/S0304-8853(99)00513-2.

(3) Portis, A. M.; Gossard, A. C. Nuclear Resonance in Ferromagnetic Cobalt. *J. Appl. Phys.* **1960**, *31* (5), S205–S213. https://doi.org/10.1063/1.1984666.